A separable cohesive element for modelling coupled failure in laminated composite materials

Lu, X.; Chen, B. Y.; Tan, V. B.C.; Tay, T. E.

DOI
10.1016/j.compositesa.2018.01.014

Publication date
2018

Document Version
Final published version

Published in
Composites Part A: Applied Science and Manufacturing

Composites Part A 107 (2018) 387–398

Contents lists available at ScienceDirect

Composites Part A

journal homepage: www.elsevier.com/locate/compositesa

A separable cohesive element for modelling coupled failure in laminated composite materials

X. Lu[a,*], B.Y. Chen[b], V.B.C. Tan[a], T.E. Tay[a]

[a] Department of Mechanical Engineering, National University of Singapore, 117576, Singapore
[b] Faculty of Aerospace Engineering, Delft University of Technology, 2629HS Delft, Netherlands

ARTICLE INFO

Keywords:
A. Fracture
B. Computational modelling
C. Laminates
D. Floating node method

ABSTRACT

A three-dimensional separable cohesive element (SCE) is proposed to enable the modelling of interaction between matrix cracking and interfacial delamination in laminated fibre-reinforced composite materials. It is demonstrated that traditional cohesive elements are incapable of modelling the coupled failure mechanisms accurately if partitioning is not allowed. The SCE may be partitioned according to the configuration and geometry of matrix cracks in adjacent plies, thus maintaining appropriate connection between plies. Physically, the original interface is split and new interfaces are formed to bond the homologous cracked solids during fracturing process. The stress concentration induced by matrix cracks and the load transfer from cracked solid elements to interface cohesive element are effectively modelled. A comprehensive set of cases of multiple matrix crack configurations from plies of different fiber angles is considered. The proposed SCE is applied to model progressive failure in composite laminates and the results are found to agree with experiments.

1. Introduction

Composite laminates are widely used in aerospace and automotive industries due to their outstanding material properties such as high strength and light weight. However, multiple failure mechanisms are often coupled when progressive damage analysis is considered. The failure process is often a combination of matrix cracking, delamination and fibre breaking, dependent on the stacking sequence and other factors. The interaction between matrix cracks and interface delamination is a major failure mechanism in composite laminates [1,2] and has been a subject of active research in recent years. Hallett et al. [3–7] conducted a series of tensile tests on notched and unnotched laminate plates, and by introducing matrix cracks into the numerical models *a priori*, better correlation with experimental results was obtained. Zubillaga et al. [8] experimentally observed that matrix cracks often trigger the onset of interlaminar delamination due to the stress concentration at the crack tips. A similar observation was found by Noh et al. [9] who predicted the shape and size of the delamination through finite element (FE) analysis. Although coupled failure behavior of composite laminates between matrix cracks and delamination has been observed in experiments, accurate modelling of this phenomenon for application in composite structures remains challenging.

In numerical progressive failure analysis, the cohesive element (CE) is commonly employed to model interface failure between different plies (i.e. delamination) of laminated composite structures [10–15]. On the other hand, intralaminar damage (i.e. matrix cracking), is often modelled with continuum damage mechanics (CDM) through smeared crack models (SCM), where degradation of stiffness is used to represent the effect of multiple micro-cracks in the plies [16–20]. The damage is assumed to be smeared out and accumulated over the FE, and an internal damage parameter is used to characterize the progressive failure process. Because the matrix cracks are not explicitly modelled, the local stress concentration and coupling between different failure modes may not be accurately described [21]. Therefore, application of these models is restricted to cases where local coupled failure mechanisms are usually not dominant. To address the limitations of SCM, alternative explicit techniques, such as extended finite element (XFEM) [22], augmented finite element (AFEM) [23], phantom node [24,25] and floating node methods (FNM) [26] have been developed. The original element is split so that matrix cracks can be explicitly introduced into the element to describe displacement discontinuity. In this way, the interaction between matrix damage and interface delamination is directly modelled [26–32]. Fang et al. [33] reported that when crack bifurcation or coalescence occurs in matrix materials, the traditional CE is unable to model the load transfer between the cohesive interface and solid elements. Therefore, a two-dimensional augmented cohesive zone (ACZ) element was proposed based on the AFEM (Fig. 1). Partitioned into two sub-elements, the ACZ element could faithfully capture the

* Corresponding author.
E-mail address: xinlu@u.nus.edu (X. Lu).

https://doi.org/10.1016/j.compositesa.2018.01.014
Received 26 October 2017; Received in revised form 4 January 2018; Accepted 15 January 2018
Available online 31 January 2018
1359-835X/

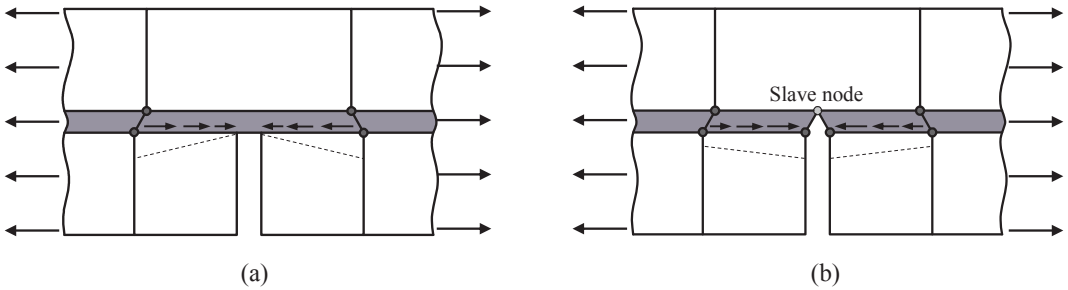

Fig. 1. ACZ element for modelling interaction between matrix crack and delamination [33]: (a) erroneous shear stress distribution by traditional CE model; (b) physically correct shear stress distribution by ACZ element model. (For interpretation of the references to colour in this figure legend, the reader is referred to the web version of this article.)

stress distribution at the interface and thus provide accurate numerical predictions. Similarly, Hu et al. enriched the CE with Heaviside function so that the CE could be split accordingly when matrix crack initiates [31]. Partitioning of CE was also achieved with additional floating nodes although these have been for interaction between single matrix crack and interface delamination only [27,28].

When multiple matrix cracks in adjacent plies with different fibre orientations are considered, the situation becomes more complicated. Cracks developed in different plies may cross each other at the shared interface, resulting in strong coupling between the interface and multiple matrix cracks. Although the phenomenon is commonly encountered in composite laminates, it has been generally neglected in most simplified analyses. In Fig. 2a, consider a case where two matrix cracks initiate in the neighboring solid elements (SE). If traditional CE is directly applied (Fig. 2b), the coupling effects caused by the cracks in plies are not correctly captured. Furthermore, although additional DoFs are introduced into the model due to the presence of the cracks, they are not properly constrained at the edges of the interface CE. Chen et al. [27] proposed an approximate solution to this problem in which overlapping two CEs with single partition is used to model the fractured interface. Although the simplified formulation can overcome some numerical difficulties, a three-dimensional SCE is required in order to physically capture the coupling behavior. As shown in Fig. 2c, the SCE should be partitioned into sub-elements in accordance with the crack configurations in the abutting SEs. Subsequent damage of the partitioned cohesive interface may thus be modelled, exhibiting the coupling between matrix cracking and interfacial delamination.

In this paper, an SCE based on FNM is developed. The proposed SCE offers several capabilities over the traditional CE:

1. It is partitionable into sub-elements according to the matrix crack configurations in neighboring SEs so that coupled failure mechanisms can be accurately modelled.
2. It is able to connect the cracked ply solids at the correct places.
3. It is able to model the delamination boundaries clearly bounded by neighboring matrix cracks.

The paper is structured as follows. The necessity for SCE is illustrated in Section 2. The detailed construction of the SCE is provided in Section 3. Several numerical examples are presented in Section 4. Finally, the conclusion is given in Section 5.

2. Necessity for three-dimensional separable cohesive element

The necessity for SCE, is demonstrated by the test problem shown in Fig. 3, where two SEs are bonded by one CE at the interface and unidirectional tensile loads are applied to the elements. (For clarity, the CE is schematically shown with a finite thickness although the actual thickness is zero.) The dimensions of the two SEs are $l \times d \times h$, the fibre directions in the top and bottom plies are α and β, respectively, and the material properties of T300/976 in Table 1 are used. Comparison between traditional CE and SCE models is shown in Fig. 4.

In the traditional CE model (Fig. 4a), after matrix cracking has occurred, the interface remains intact and connected to the cracked SEs. However, the CE is under in-plane stretch deformation and no force is generated within the element. It does not directly experience the effect of the matrix cracks above and below, and thus does not participate in any load transfer. Throughout the entire process, the traditional CE makes no contributions towards bearing the external loads and only matrix damage is predicted (Fig. 4a).

In the SCE model, the interface the CE is partitioned according to the crack configurations in its neighboring SEs, as shown in Fig. 4b. The stresses released by the cracked SEs are concentrated and transferred into the triangular sub-CEs through shear deformation. Failure of these two triangular sub-CEs (delamination) and matrix cracking constitute final fracture. Significant differences are observed from the predicted load-displacement curves of the two models (Fig. 4c). Higher strength is predicted by the SCE model compared to the traditional CE model where only matrix cracking is captured.

Detailed elemental analyses with various fibre angles are provided

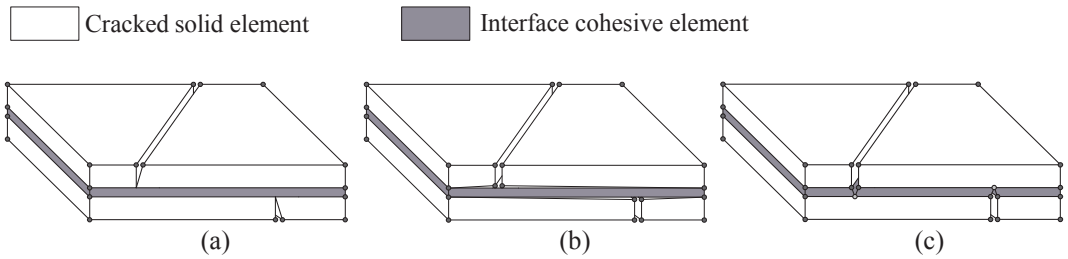

Fig. 2. Three-dimensional coupling between matrix cracks and delamination: (a) two matrix cracks initiate in adjacent plies; (b) traditional CE fails to capture coupling between matrix cracks and interface failure; (c) SCE models the interaction between matrix cracking and delamination. (For interpretation of the references to colour in this figure legend, the reader is referred to the web version of this article.)

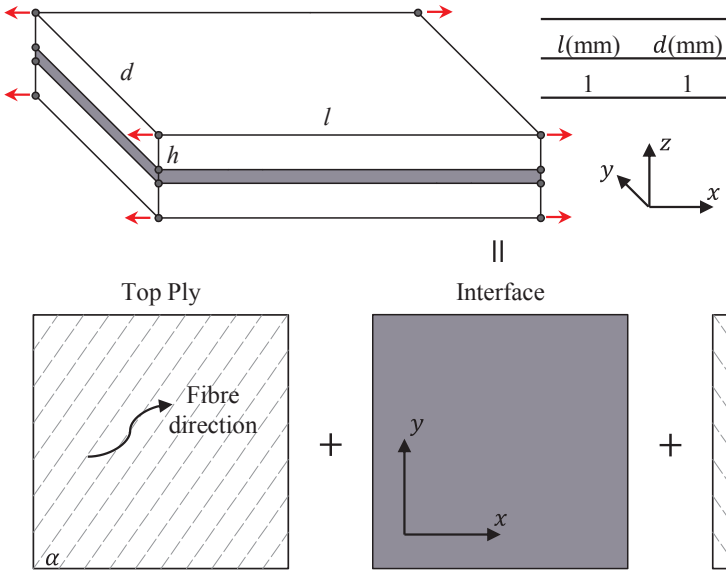

l(mm)	d(mm)	h(mm)	α(°)	β(°)
1	1	0.1	-75	75

Fig. 3. Numerical model of two ply SEs bonded by one interface CE subjected to uniaxial tensile load. (For interpretation of the references to colour in this figure legend, the reader is referred to the web version of this article.)

in Fig. 5. Without capturing the delamination failure properly, the traditional CE models under-predict the material capabilities in element level. However, it is shown that the SCE formulation results in higher maximum load due to the proper accounting of the load transfer.

3. 3D separable cohesive element

In this section, the FNM proposed in [27,28,34] which explicitly models the matrix cracks and delamination is briefly reviewed, and based on the same framework, the 3D SCE is formulated. All possible coupling scenarios between matrix cracking and interfacial delamination are considered when developing the SCE. The proposed SCE can be employed in an unstructured mesh with arbitrary propagation of a large number of matrix cracks.

3.1. Overview of the Floating Node Method (FNM)

In this paper, the FNM is adopted to formulate the SCE (Fig. 6). In order to model crack propagation and crack-induced discontinuities within existing elements, additional floating nodes are allocated in the element formulation. Before matrix cracking, the floating nodes (and the associated floating DoFs) are not used in the analysis, and hence the

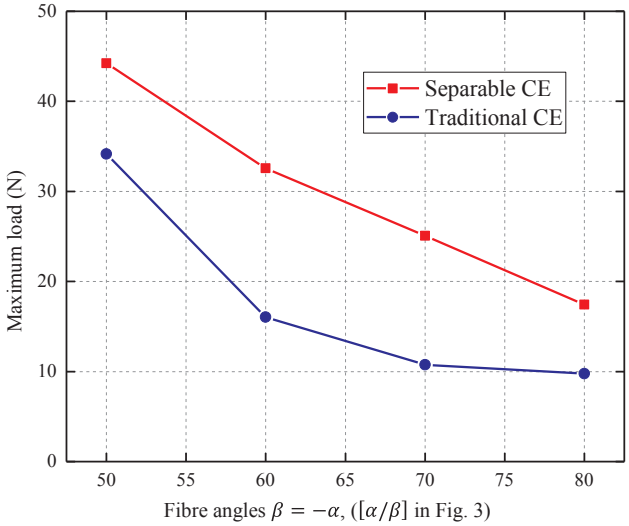

Fig. 5. Predicted maximum load in elemental analysis with different fibre angles. (For interpretation of the references to colour in this figure legend, the reader is referred to the web version of this article.)

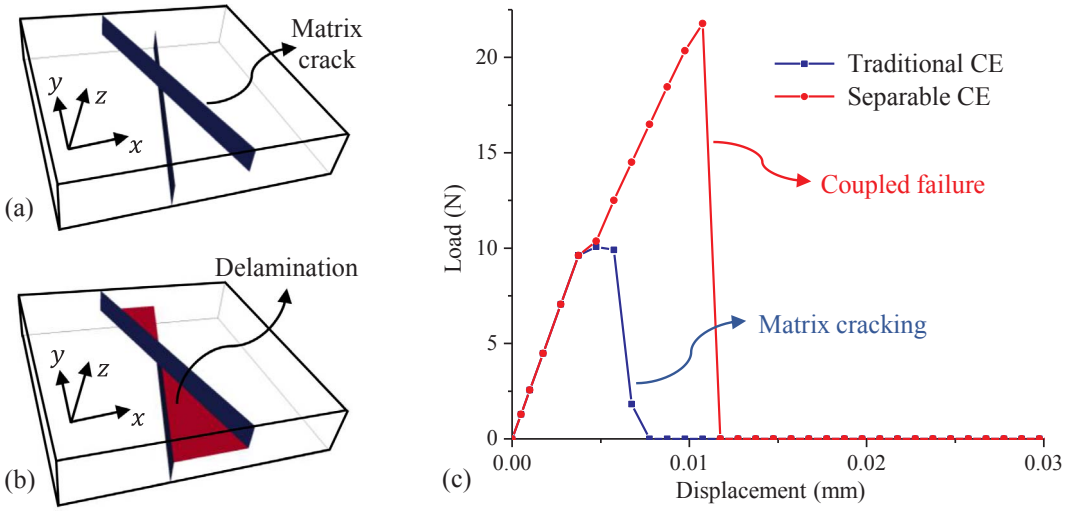

Fig. 4. Comparison of numerical results between traditional CE and SCE: (a) final failure pattern of traditional CE model; (b) final failure pattern of SCE model; (c) load-displacement curves. (For interpretation of the references to colour in this figure legend, the reader is referred to the web version of this article.)

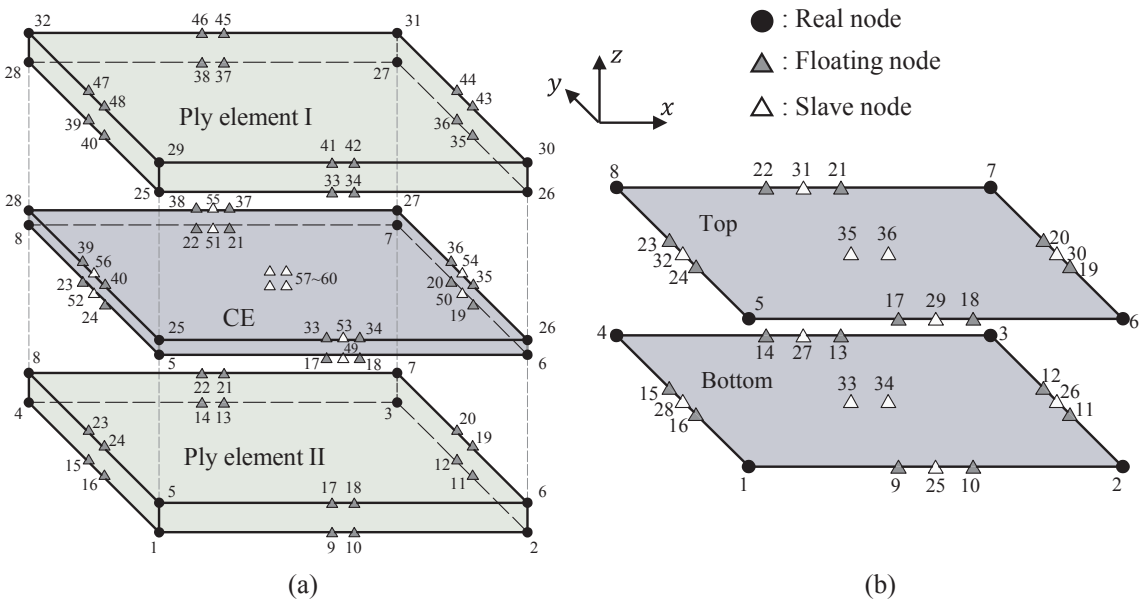

Fig. 6. Floating node element (a) a two-ply laminate element; (b) the interface cohesive element. (For interpretation of the references to colour in this figure legend, the reader is referred to the web version of this article.)

ply elements are simply standard solid elements. When matrix cracking is predicted through satisfying the failure criterion, these floating nodes are activated and assigned to the positions where the cracks occur. The ply element is then partitioned into several sub-elements and CE may be inserted in between to model cracks. Further details of the FNM can be found in [26–28].

3.2. Separable cohesive element

In this section, formulation of the SCE is presented. As shown in Fig. 6a, two ply elements sandwich the SCE in between. By sharing the nodes from solid elements, the bottom surface of ply element I forms the top surface of the CE, while the top surface of ply element II forms the bottom surface of the CE. Fig. 6b shows the local nodal connectivity of the SCE: nodes 1–24 are the common nodes from neighboring SEs while nodes 25–32 are edge slave nodes and nodes 33–34 are surface slave nodes. The real and floating nodes are used to construct or partition the CE, while the slave nodes are used to ensure compatibility is preserved.

3.2.1. Before matrix cracking

Prior to matrix cracking, both ply elements are intact and the floating nodes are not included in the calculations. Only the real nodes (1–8) are used to form the interface CE and the derivation of stiffness matrix of the CE is given as follows [35].

The separations between top and bottom surfaces of the CE are related to the homologous displacements (Fig. 6):

$$\widetilde{\boldsymbol{\delta}} = \widetilde{\boldsymbol{u}}^{top} - \widetilde{\boldsymbol{u}}^{bot} \tag{1}$$

where $\widetilde{\boldsymbol{\delta}} = [\widetilde{\delta}_n, \widetilde{\delta}_t, \widetilde{\delta}_l]'$ and $\widetilde{\boldsymbol{u}} = [\widetilde{u}_n, \widetilde{u}_t, \widetilde{u}_l]'$ are displacement components in the local coordinate system. The subscripts n, t and l represent normal, transverse and longitudinal directions to the surface of CE, while the superscripts *top* and *bot* represent top and bottom surfaces of the CE, respectively.

The displacement field $\boldsymbol{u}$ can be interpolated by the nodal displacements in global coordinate system:

$$\boldsymbol{u} = \boldsymbol{N}\boldsymbol{u}_n \tag{2}$$

where $\boldsymbol{N}$ is the shape function matrix and $\boldsymbol{u}_n$ is the corresponding nodal displacement vector.

Through the transformation matrix $\boldsymbol{R}$ between global and local coordinate systems, the vector of separations can be rewritten as:

$$\begin{aligned}\widetilde{\boldsymbol{\delta}} &= \boldsymbol{R}(\boldsymbol{N}^{top}\boldsymbol{u}_n^{top} - \boldsymbol{N}^{bot}\boldsymbol{u}_n^{bot}) \\ &= \boldsymbol{R}[-\boldsymbol{N}^{bot}\ \boldsymbol{N}^{top}][\boldsymbol{u}_n^{bot}\ \boldsymbol{u}_n^{top}]' \\ &= \boldsymbol{B}\boldsymbol{u}_n\end{aligned} \tag{3}$$

The tractions in the CE can be calculated from the separations [36]:

$$\widetilde{\tau} = \widetilde{\boldsymbol{D}}\widetilde{\boldsymbol{\delta}} \tag{4}$$

where $\widetilde{\boldsymbol{D}}$ is the constitutive matrix derived from the cohesive law.

Through the weak formulation of the virtual work principle, the stiffness matrix of the CE is given by:

$$\boldsymbol{K} = \int_{-1}^{1}\int_{-1}^{1} \boldsymbol{B}'\widetilde{\boldsymbol{D}}\boldsymbol{B}\left(\det\boldsymbol{J}\right)d\xi d\eta \tag{5}$$

where $\boldsymbol{J}$ is the Jacobian matrix; ξ and η are coordinates in natural (isoparameter) coordinates.

3.2.2. Single matrix crack

Consider a case in which two ply SEs are bonded by an interface CE (Fig. 7a). When a matrix crack initiates or propagates within one of the plies, e.g. the top ply SE, floating nodes on the cracked edges are activated to partition the ply element (Fig. 7b). The top surface of the CE is partitioned accordingly by the same activated floating nodes, while the bottom surface of the CE remains intact. To complete the CE formulation, the intact bottom surface of the CE must be seeded with slave nodes (dashed line in Fig. 7c). Therefore, the original CE is separated into two sub-CEs, elements ① and ② in Fig. 7c:

$$\begin{aligned}&\boldsymbol{CE}_1\text{: }\{1,25,27,4,5,17,22,8\} \\ &\boldsymbol{CE}_2\text{: }\{25,2,3,27,18,6,7,21\}\end{aligned} \tag{6}$$

Eq. (6) describes the local nodal connectivity of the sub-CEs, where

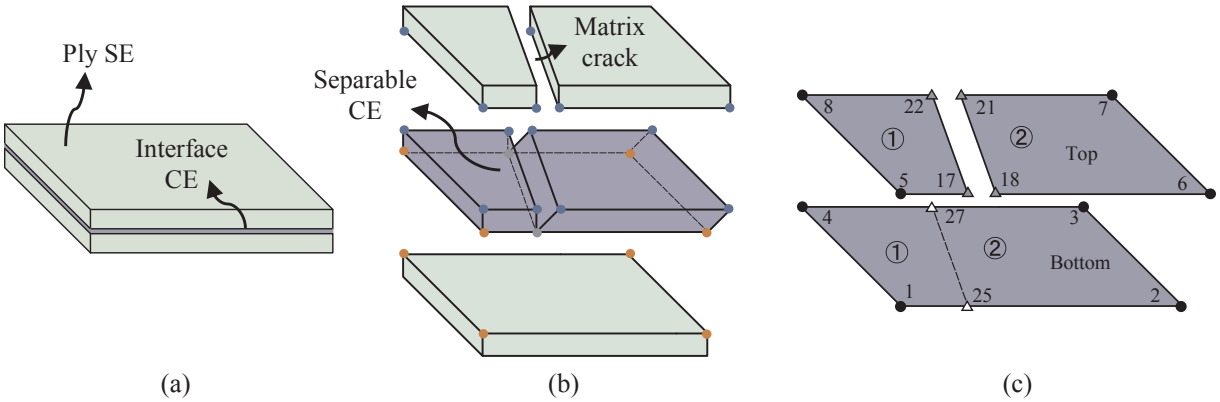

Fig. 7. Single matrix crack in two-ply laminate element: (a) Two-ply laminate element with two ply SEs bonded by an interface CE; (b) single matrix crack developed in the top ply element; (c) SCE and nodal connectivity. (For interpretation of the references to colour in this figure legend, the reader is referred to the web version of this article.)

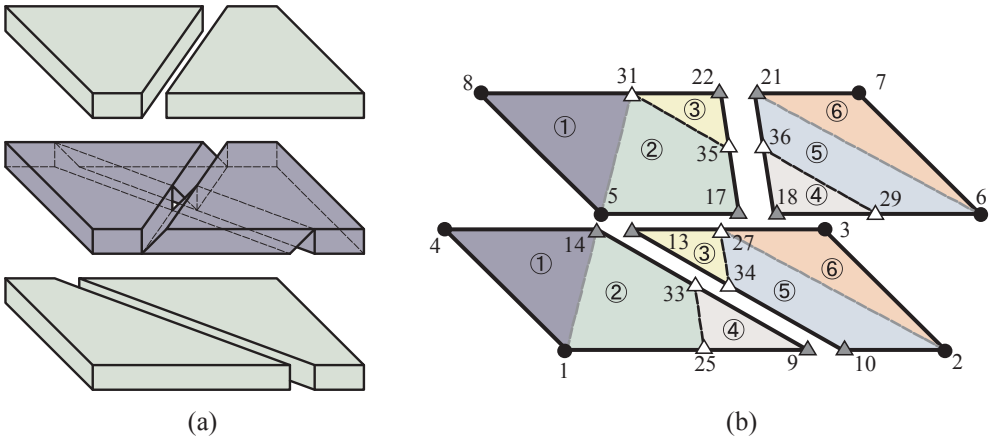

Fig. 8. Multiple matrix cracks in two-ply laminate element: (a) two matrix cracks developed in both top and bottom ply elements; (b) SCE and nodal connectivity. (For interpretation of the references to colour in this figure legend, the reader is referred to the web version of this article.)

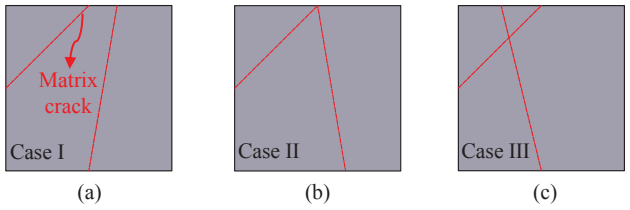

Fig. 9. 2D views of all possible cases with two matrix cracks in one CE: (a) case I, intersection out of the element; (b) case II, intersection on element edge; (c) case III, intersection inside the element. (For interpretation of the references to colour in this figure legend, the reader is referred to the web version of this article.)

nodes 1–8 are the real nodes; nodes 17, 18, 21 and 22 are the floating nodes activated to partition the cracked top surface; nodes 25 and 27 are the slave nodes used to divide the intact bottom surface and define the proper integration domains for the sub-CEs. The numbering order of the nodes follows the configuration in Fig. 6b.

Note that since the bottom surface of CE is not really fractured, its configuration is determined by the corner nodes of the bottom ply element (nodes 1–4 in Fig. 7c). Therefore, the slave nodes 25 and 27 and their associated DoFs do not enter into the element formulation. To preserve compatibility, the slave nodes are constrained at the edges and their DoFs $\boldsymbol{u}_{25}$ and $\boldsymbol{u}_{27}$ are related to the DoFs of the real nodes through interpolation:

$$\begin{aligned}\boldsymbol{u}_{25} &= N_1(\boldsymbol{x}_{25})\boldsymbol{u}_1 + N_2(\boldsymbol{x}_{25})\boldsymbol{u}_2 \\ \boldsymbol{u}_{27} &= N_3(\boldsymbol{x}_{27})\boldsymbol{u}_3 + N_4(\boldsymbol{x}_{27})\boldsymbol{u}_4\end{aligned} \tag{7}$$

where N_i is the shape function for node i.

After partitioning, the stiffness matrices of the two sub-elements can be calculated by Eq. (5):

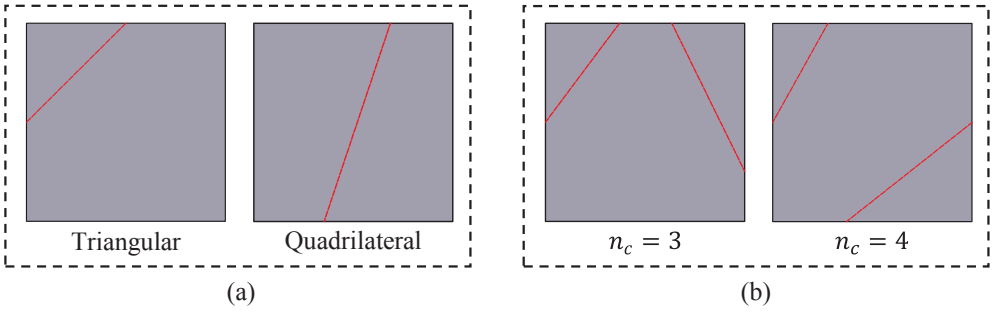

Fig. 10. Factors to differentiate sub-cases: (a) shape of the sub-CE; (b) number of the cracked edges. (For interpretation of the references to colour in this figure legend, the reader is referred to the web version of this article.)

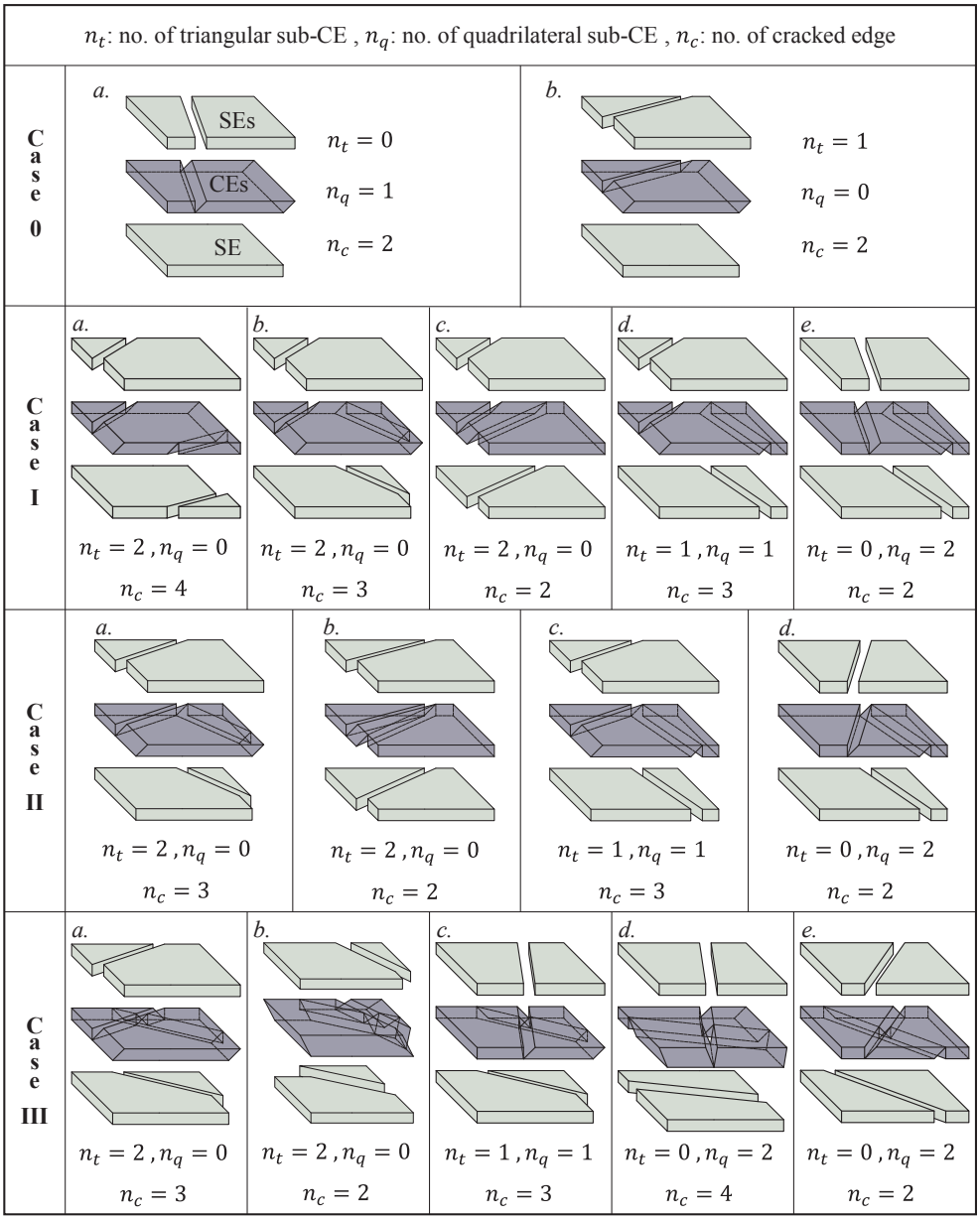

Fig. 11. All the possible cases of SCE modelling interaction between matrix cracks and interface delamination. (For interpretation of the references to colour in this figure legend, the reader is referred to the web version of this article.)

$$\boldsymbol{K}_1 = \int_{-1}^{1}\int_{-1}^{1} \boldsymbol{B}_1' \widetilde{\boldsymbol{D}} \boldsymbol{B}_1 (\det \boldsymbol{J}_1) d\xi_1 d\eta_1$$
$$\boldsymbol{K}_2 = \int_{-1}^{1}\int_{-1}^{1} \boldsymbol{B}_2' \widetilde{\boldsymbol{D}} \boldsymbol{B}_2 (\det \boldsymbol{J}_2) d\xi_2 d\eta_2 \quad (8)$$

where the variables with subscript i are defined for sub-element i. The stiffness matrices given by Eq. (8) are finally assembled into the overall stiffness matrix of the SCE:

$$\boldsymbol{K}_{CE} = \mathcal{A}(\boldsymbol{K}_1, \boldsymbol{K}_2) \quad (9)$$

where $\mathcal{A}$ is the assembly operator. The slave nodes and the associated DoFs can be removed from the stiffness matrix $\boldsymbol{K}_{CE}$ using master-slave constraints according to Eq. (7).

3.2.3. Multiple matrix cracks

When both top and bottom ply SEs are fractured, interaction between two cracks should be considered when constructing the SCE. Fig. 8a shows a situation where two matrix cracks from adjacent plies intersect at the cohesive interface. The SCE should be partitioned according to matrix cracks in the abutting SEs. In Fig. 8a, the interface is divided into four parts to ensure that the cracked solid domains remain bonded to the sub-interfaces. The element formation is shown in Fig. 8b. For FE implementation, the pentagonal interface is further partitioned into triangular and quadrilateral sub-CEs. The SCE is thus divided into six sub-elements (Fig. 8b) as follows:

$\boldsymbol{CE}_1$: {1,14,4,5,31,8}
$\boldsymbol{CE}_2$: {1,25,33,14,5,17,35,31}
$\boldsymbol{CE}_3$: {34,27,13,35,22,31}
$\boldsymbol{CE}_4$: {25,9,33,18,29,36}
$\boldsymbol{CE}_5$: {10,2,27,34,29,6,21,36}
$\boldsymbol{CE}_6$: {2,3,27,6,7,21} (10)

The displacements of slave nodes on element edges are obtained by interpolation of values at the corner nodes:

$$\boldsymbol{u}_{25} = \frac{d_{9,25}}{d_{1,9}}\boldsymbol{u}_1 + \frac{d_{1,25}}{d_{1,9}}\boldsymbol{u}_9,\ \boldsymbol{u}_{27} = \frac{d_{13,27}}{d_{3,13}}\boldsymbol{u}_3 + \frac{d_{3,27}}{d_{3,13}}\boldsymbol{u}_{13}$$
$$\boldsymbol{u}_{29} = \frac{d_{18,29}}{d_{6,18}}\boldsymbol{u}_6 + \frac{d_{6,29}}{d_{6,18}}\boldsymbol{u}_{18},\ \boldsymbol{u}_{31} = \frac{d_{22,31}}{d_{8,22}}\boldsymbol{u}_8 + \frac{d_{8,31}}{d_{8,22}}\boldsymbol{u}_{22} \tag{11}$$

where $d_{i,j}$ is the distance between nodes i and j. Slave nodes 33–36 are used for the intersection of two matrix cracks and the associated DoFs can be calculated through the displacements of corner nodes on crack surfaces:

$$\boldsymbol{u}_{33} = \frac{d_{14,33}}{d_{9,14}}\boldsymbol{u}_9 + \frac{d_{9,33}}{d_{9,14}}\boldsymbol{u}_{14},\ \boldsymbol{u}_{34} = \frac{d_{13,34}}{d_{10,13}}\boldsymbol{u}_{10} + \frac{d_{10,34}}{d_{10,13}}\boldsymbol{u}_{13}$$
$$\boldsymbol{u}_{35} = \frac{d_{22,35}}{d_{17,22}}\boldsymbol{u}_{17} + \frac{d_{17,35}}{d_{17,22}}\boldsymbol{u}_{22},\ \boldsymbol{u}_{36} = \frac{d_{21,36}}{d_{18,21}}\boldsymbol{u}_{18} + \frac{d_{18,36}}{d_{18,21}}\boldsymbol{u}_{21} \tag{12}$$

The stiffness matrix $\boldsymbol{K}_i$ for sub-CE i can be calculated by Eq. (5) in the corresponding sub-domain (with $i = 1 \sim 6$). The overall stiffness matrix is given by:

$$\boldsymbol{K}_{CE} = \mathcal{A}(\boldsymbol{K}_1,\boldsymbol{K}_2,\boldsymbol{K}_3,\boldsymbol{K}_4,\boldsymbol{K}_5,\boldsymbol{K}_6) \tag{13}$$

Using Eqs. (11) and (12), the slave nodal DoFs are removed from the stiffness matrix $\boldsymbol{K}_{CE}$.

3.3. All the possible scenarios

In failure analysis of composite laminates, a large number of matrix cracks may develop. Therefore, all possible cases of intersecting cracks should be considered in formulating the SCE. The scenarios where single crack exists in the CE have been addressed in [27]. In this section, only those with two cracks are considered. Fig. 9a–c are two-dimensional views of the interface CE, where the red lines represent projections of the matrix cracks from neighboring ply elements. As shown in Fig. 9, there are three possibilities:

1. Case I, the intersection of two matrix crack is outside the element (Fig. 9a).
2. Case II, two matrix cracks meet each other at one of the element edges (Fig. 9b).
3. Case III, two cracks intersect within the element (Fig. 9c).

Although the above three cases are in general sufficient to include all possibilities, for FE implementation, several sub-cases are examined considering various crack configurations. Two factors are considered to distinguish these sub-cases: the shape of sub-CE and the number of cracked edges. As shown in Fig. 10a, if the crack cuts two neighboring edges, the original CE is divided into one triangular and one pentagonal sub-element, while if the crack cuts two opposite edges, two quadrilateral sub-elements will be obtained. The number of cracked edges, n_c, can be illustrated through Fig. 10b. For the first figure of Fig. 10b, three edges are cracked while for the second one, four edges are cracked. Hence, n_c will be 3 and 4, respectively.

Fig. 11 shows all the possible cases of the SCE. Case 0 stands for the situation where only one crack exists in one of two abutting ply SEs; Cases I - III correspond to cases involving two cracks (Fig. 9). Taking into account the shape of sub-CEs and number of cracked edges, each case can be further classified into several sub-types.

3.4. Failure models

In this section, the failure criteria adopted in the numerical analysis examples for fibre failure, matrix cracks and delamination are briefly introduced. The details can be found in [27]. The maximum stress criterion is adopted to predict the onset of fibre tensile failure:

$$\frac{\sigma_1}{X_t} = 1 \tag{14}$$

where X_t is the tensile strength in fibre direction. The cohesive zone model is used to model the damage evolution of fibre failure:

$$\int_0^{u_1^f} \sigma_1 du_1 = \frac{1}{2} X_t u_1^f = G_{fc} \tag{15}$$

where u_1^f is the final failure displacement in fibre direction and G_{fc} is the fracture toughness.

The initiation of matrix-dominated tensile failure is predicted by the quadratic criterion based on the normal and shear tractions:

$$\left(\frac{\tau_n}{\tau_n^c}\right)^2 + \left(\frac{\tau_t}{\tau_t^c}\right)^2 + \left(\frac{\tau_l}{\tau_l^c}\right)^2 = 1 \tag{16}$$

where τ_i represents traction in i direction and τ_i^c is the corresponding strength. The damage evolution of the CE follows a mixed-mode bilinear cohesive law:

$$\int_0^{\delta_e^f} \tau_e d\delta_e = \frac{1}{2}\tau_e^{max}\delta_e^f = G_{mc} \tag{17}$$

where:

$$\delta_e = \sqrt{<\delta_n>^2 + \delta_t^2 + \delta_l^2}$$
$$\tau_e = \frac{(\tau_n < \delta_n > + \tau_t\delta_t + \tau_l\delta_l)}{\delta_e}$$
$$<\delta_n> = \max(0,\delta_n) \tag{18}$$

and G_{mc} is the mixed-mode fracture toughness:

$$G_{mc} = \left[\left(\frac{\lambda_n}{G_{nc}}\right)^\alpha + \left(\frac{\lambda_t}{G_{tc}}\right)^\alpha + \left(\frac{\lambda_l}{G_{lc}}\right)^\alpha\right]^{-1/\alpha} \tag{19}$$

and α is the power law exponent and G_{ic} is the fracture toughness in i direction. λ_i is calculated by:

$$\lambda_i = \frac{G_i}{G_m},\ G_m = \sum_i G_i \tag{20}$$

with $G_i = \tau_i\delta_i$ at the failure onset.

The same criterion and cohesive law (Eq. (16)–(20)) are adopted to model the onset and evolution of interface delamination.

4. Numerical verifications

The SCE is developed in Abaqus FE software (Implicit, version 6.14) as a user-defined element. The performance of the SCE is verified through numerical simulations of tensile failure of unnotched $[30/90/-30]_s$ T300/976 laminates [1,2] and notched $[45_4/90_4/-45_4/0_4]_s$

Table 1
Material properties of T300/976 [2,27,41] and IM7/8552 [5].

Properties	T300/976	IM7/8552
Longitudinal Young's modulus: E_1 (GPa)	139.2	161
Transverse Young's modulus: E_2, E_3 (GPa)	9.7	11.4
Shear modulus: G_{12}, G_{13} (GPa)	5.5	5.17
Shear modulus: G_{23} (GPa)	3.4	3.98
Poisson's ratio: ν_{12}, ν_{13}	0.29	0.32
Poisson's ratio: ν_{23}	0.4	0.43
Longitudinal tensile strength: X_t (MPa)	1515	2806
Transverse tensile strength: τ_{nc} (MPa)	45	60
Shear strength: τ_{tc}, τ_{lc} (MPa)	100	90
Interfacial normal strength*: $\tau_{nc,dlm}$ (MPa)	22.5	30
Interfacial shear strength*: $\tau_{tc,dlm}$, $\tau_{lc,dlm}$ (MPa)	50	45
Mode I matrix fracture toughness: G_{nc} (kJ/m^2)	0.158	0.293
Mode II matrix fracture toughness: G_{tc}, G_{lc} (kJ/m^2)	0.35	0.631
Mode I interfacial fracture toughness: $G_{nc,dlm}$ (kJ/m^2)	0.158	0.293
Mode II interfacial fracture toughness: $G_{tc,dlm}$, $G_{lc,dlm}$ (kJ/m^2)	0.315	0.631
Power-law exponent for mixed-mode fracture: α	1	1
Penalty stiffness (N/mm^3)	10^6	10^6

* Reduced interfacial strengths adopted for feasible mesh sizes [15,38–40].

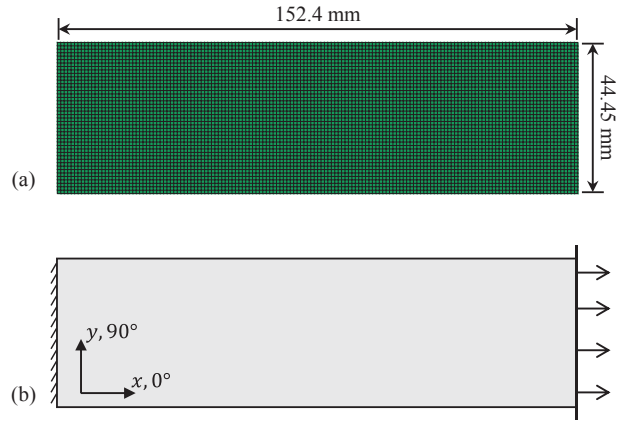

Fig. 12. Unnotched laminated plate: (a) sample dimensions and FE mesh; (b) boundary conditions for unidirectional tension. (For interpretation of the references to colour in this figure legend, the reader is referred to the web version of this article.)

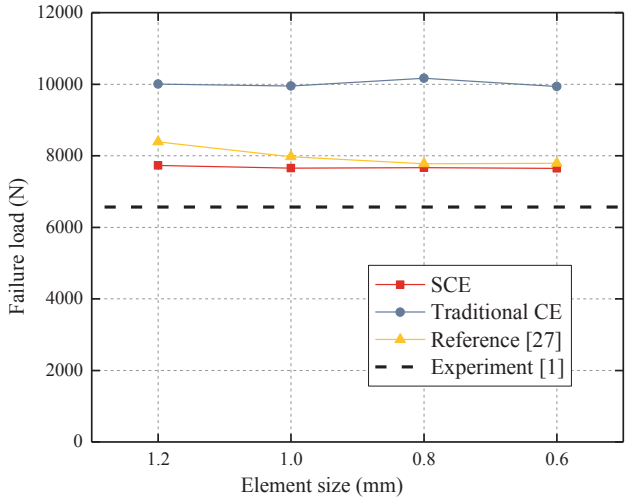

Fig. 13. Mesh-refinement: predicted failure load with various element sizes. (For interpretation of the references to colour in this figure legend, the reader is referred to the web version of this article.)

IM7/8552 laminates [5]. The material properties adopted for FE analysis are given in Table 1. Generally, if fine meshes are adopted, the values for the interfacial and transverse strengths are assumed to be the same [3,21,37]. However, over-prediction of the structural strengths is expected if the element size is insufficiently small, and to get satisfactory results with relatively coarse CE meshes, reduced interfacial strengths are sometimes recommended [15,38–40]. In the present paper, the strengths are reduced with a factor 2 (i.e., the interfacial strengths are half of the transverse strengths), which is suggested by van der Meer et al. [40].

4.1. *Tensile failure of unnotched* $[30/90/-30]_s$ *laminate*

To study the coupled failure of composite laminates, the unnotched $[30/90/-30]_s$ laminate loaded in tension in [1] is modelled. The experimental results showed that before abrupt catastrophic failure, the damage in the laminate consisted of small edge delamination bounded by short matrix cracks [1]. This observation indicated the strong coupling between intralaminar damage and interlaminar delamination during the progressive failure of the composite laminate.

The FE model and the boundary conditions (BCs) are shown in Fig. 12. Due to the symmetric layup, only half of the laminated plate is modelled; symmetric BCs are applied to the laminate mid-plane. Employing structured mesh with uniform element size, a mesh-refinement test is performed (Fig. 13) for four different mesh sizes, i.e., 1.2 mm, 1 mm, 0.8 mm and 0.6 mm. Apart from the proposed SCE, the traditional CE and simplified formulation (overlapping two partitioned CEs [27]) are also studied. Simply applying the traditional CE leads to significant over-predictions of the failure load (51% compared to experiment with 1 mm mesh), while satisfactory results are obtained with the approximate method (21% with 1 mm mesh). However, the accuracy is further improved (16% with 1 mm mesh) if the proposed SCE is adopted.

Overall, the predicted failure process and damage patterns are insensitive to the mesh size. In the following numerical failure profiles, delamination is represented by red area while matrix cracks are represented by straight lines (Figs. 14 and 15). The numerical results show that matrix cracks initiate firstly on the free edge of the middle 90° ply, and through the separated CEs, the loads released from the cracked solids are transferred to the neighboring ± 30° plies, triggering onset of new intralaminar damage in those plies. At the same time, 30°/90° and 90°/-30° interfacial delamination initiates near the intersection of matrix cracks due to the stress concentrations. As the loading continues, triangular delamination is predicted at the free edges, bounded by the 30° and -30° matrix cracks in the adjacent plies (Figs. 14 and 15a). This failure pattern reveals the coupled damage mechanisms in composite laminates, as observed in experimental studies [1,3,8]. Adopting the SCEs in the simulation, the delamination boundaries are clearly observed and compared to the experimental X-radiograph [1], close agreement is achieved (Fig. 14).

For comparison, the same analysis but with traditional CE (i.e. no partitioning) and approximate approach in [27] is conducted (Fig. 15b and c). In this case, extensive matrix cracks develop throughout the whole laminate at initial stage; however, without correctly modelling the load transfer, the induced delamination is not observed and only a small area of free-edge delamination is predicted when the peak load is reached (Fig. 15b). The longer matrix cracks predicted and the delayed onset of delamination account for the over-estimation of the failure load (Fig. 13). Although the approximate formulation [27] avoids spurious prediction of matrix cracks, there is fewer delamination predicted at the initial stage when compared to the current SCE formulation (Fig. 15c). Also, the delamination in the approximate formulation are not accurately bounded by the matrix cracks, which is the situation with the SCE formulation and observed experimentally.

The results show that traditional CE fails to capture the interaction between matrix cracking and delamination and the approximate formulation of [27] only approximately captures this interaction, while such coupling is accurately described by the proposed SCE.

4.2. *Tensile failure of notched* $[45_4/90_4/-45_4/0_4]_s$ *laminate*

The open-hole tension (OHT) of $[45_4/90_4/-45_4/0_4]_s$ laminate plate [5] is analyzed in this section. The FE model and the boundary conditions (BCs) are shown in Fig. 16. A random unstructured mesh is adopted, where the elements are about 0.5 mm × 0.5 mm in the region near the hole and 1 mm × 1 mm in the remaining regions (Fig. 16a). Only half of the laminate plate is modelled and tensile load is applied (Fig. 16b). Analysis using traditional CE and SCE are performed for comparison (detailed discussions on the approximate formulation can be found in [27]).

The predicted strengths of the laminate are 285 MPa for SCE model and 289 MPa for traditional CE model, which agree well with the experimental average of 275 MPa. In terms of the failure loads, no

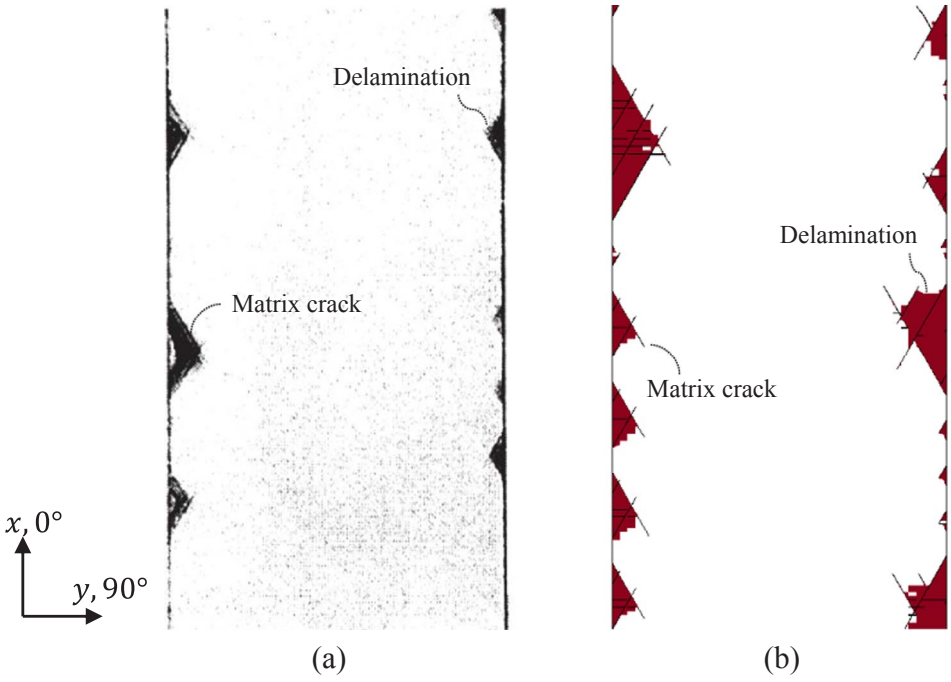

Fig. 14. Comparison between experimental observations and numerical predictions: (a) X-radiograph of damaged sample [1]; (b) FE results using SCEs (1 mm mesh). (For interpretation of the references to colour in this figure legend, the reader is referred to the web version of this article.)

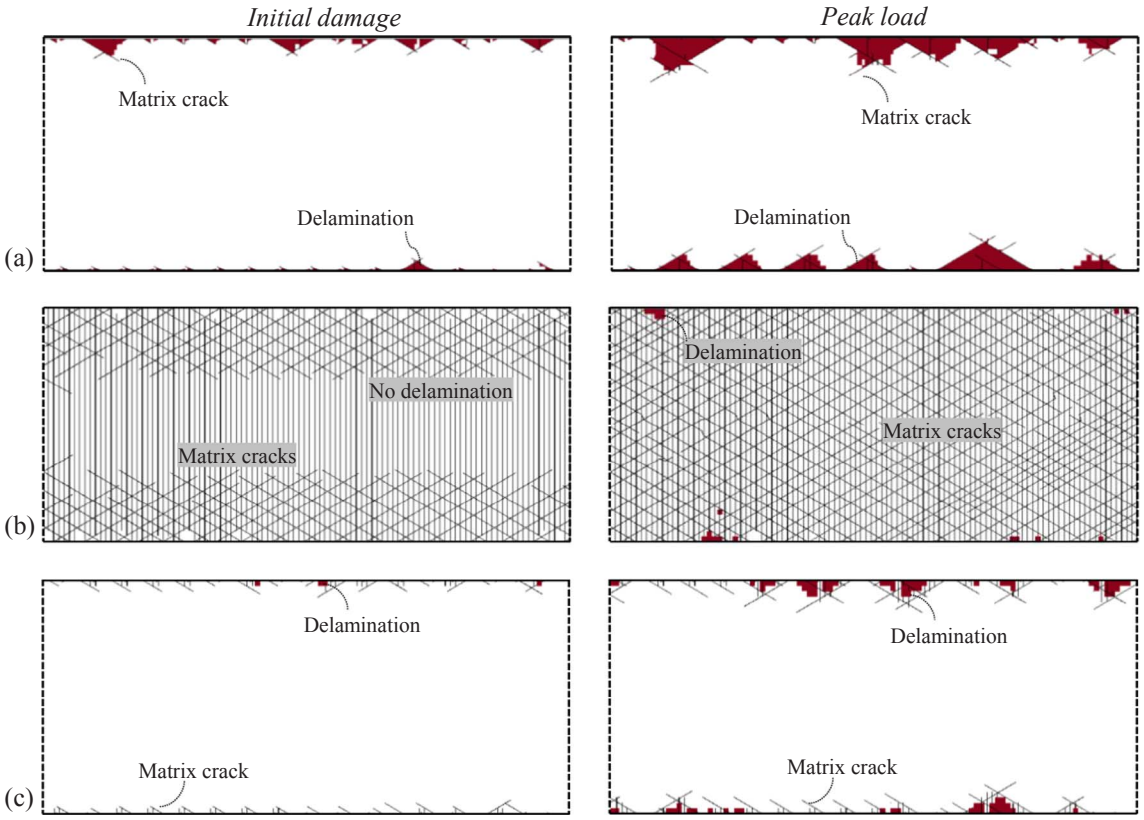

Fig. 15. Numerical results of unnotched $[30/90/-30]_s$ laminate plate for initial damage (left column) and peak load damage (right column): (a) model with SCE; (b) model with traditional CE; (c) model with simplified formulation [27]. (For interpretation of the references to colour in this figure legend, the reader is referred to the web version of this article.)

significant improvement is achieved by employing the SCE.

From the experimental X-radiographs in [17], boundaries of the delamination, which align with matrix cracks, are clearly observed (Fig. 17a), indicating a coupled failure process. Employing the SCEs, the boundaries of the delamination are clearly defined and good agreement with experiment is achieved (Fig. 17b). However, if traditional CEs are adopted, the predicted delamination boundaries appear to be influenced by the FE mesh (Fig. 17c).

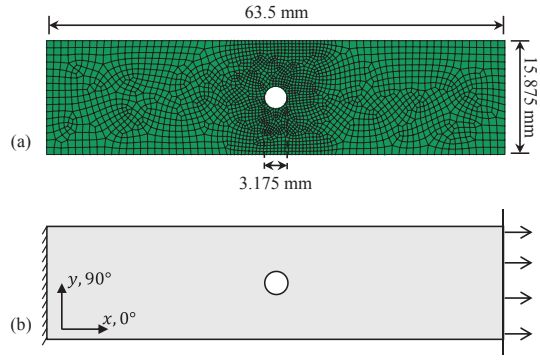

Fig. 16. Open-hole laminate plate: (a) sample dimensions and FE mesh; (b) boundary conditions for unidirectional tension. (For interpretation of the references to colour in this figure legend, the reader is referred to the web version of this article.)

The overall failure patterns including matrix cracking and interfacial delamination predicted by both models are shown in Fig. 18. Matrix cracking triggers the onset of interface delamination, and *vice versa* [5,6]. In the case where SCEs are used, the matrix cracks and delamination are better defined and the prediction patterns are in better agreement with experiments (Fig. 18a). On the other hand, in the case of conventional CEs, a large number of isolated matrix cracks, particularly at the edges, is predicted in the region away from the hole (Fig. 18b).

Although both the SCE and traditional CE approaches seem to provide similar results for the OHT test on final failure loads and profiles (Figs. 17 and 18), the initial damage progression reveals significant differences between the two models (Fig. 19). Due to the presence of the open hole, the stress concentration triggers the onset of matrix damage. If SCE is employed, the newly developed matrix cracks rapidly induce local delamination in the abutting interfaces. The matrix cracks and delamination then propagate simultaneously as the loading continues (Fig. 19a). In contrast, with traditional CE, no delamination is observed until the surface 45° matrix cracks propagate across the width of the plate (Fig. 19b). In this case, the delamination is mainly caused by overall structural behavior rather than local coupling effects.

5. Conclusion

In this paper, the 3D separable cohesive element (SCE) is proposed for modelling the coupled failure of composite laminates. When matrix cracks initiate or propagate in the ply solid elements (SEs), the associated SCE is partitioned into several individual sub-CEs to maintain the correct bonding between the cracked solids. Depending on various crack geometries in the abutting plies, different elemental configurations are categorized and formulated for implementation in FE.

The interactions between matrix cracking and interfacial delamination can be properly modelled with SCEs. This has been demonstrated through several numerical examples, where delamination boundaries are better defined and fewer spurious matrix cracks are predicted compared to models employing only traditional CEs.

For unnotched laminates, the SCE model successfully captures the predicted failure load and the local delamination induced by matrix

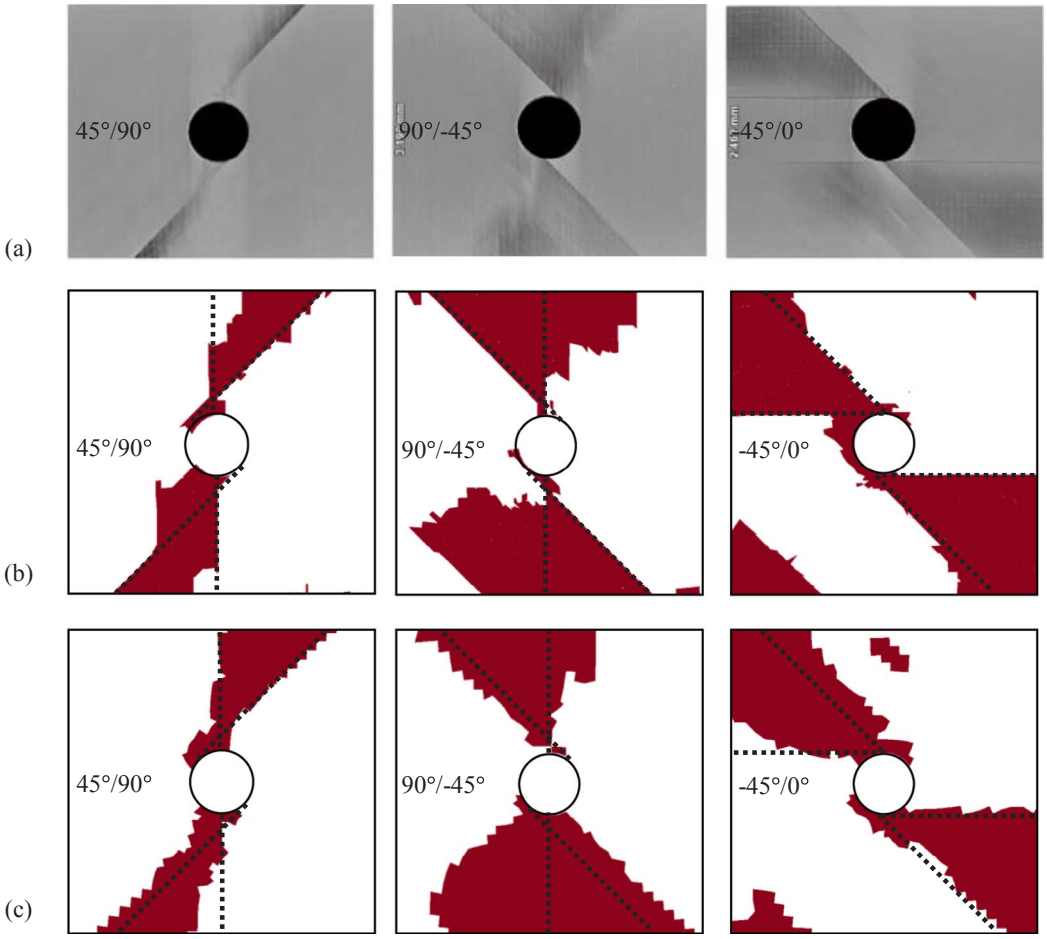

Fig. 17. Comparisons of delamination patterns of $[45_4/90_4/-45_4/0_4]_s$ open-hole plate: (a) X-radiographs of delamination patterns on three interfaces [17]; (b) simulated delamination patterns with SCE model; (c) simulated delamination patterns with traditional CE model. (For interpretation of the references to colour in this figure legend, the reader is referred to the web version of this article.)

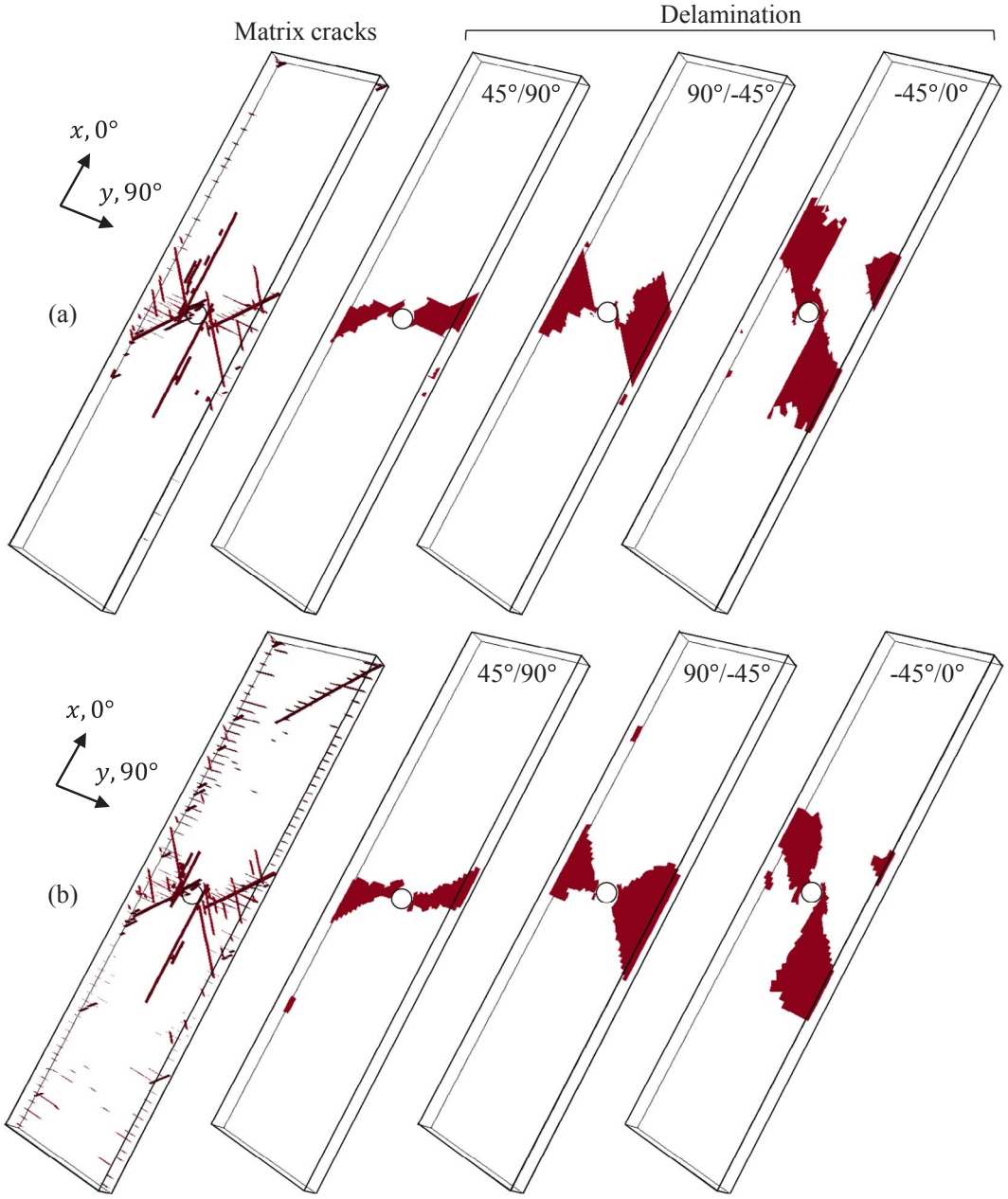

Fig. 18. Comparisons of the overall damage patterns of $[45_4/90_4/-45_4/0_4]_s$ open-hole plate: (a) matrix cracks and delamination with SCE model; (b) matrix cracks and delamination with traditional CE model. (For interpretation of the references to colour in this figure legend, the reader is referred to the web version of this article.)

cracks, in close agreement with experimental observations. However, the differences in employing the SCE and traditional CE are not that obvious when considering the OHT test. This may be due to the fact that damage initiation is dominated by the stress concentration at the open hole edge, and less affected by local interactions between matrix and interface delamination. Nonetheless, it is worth noting that more faithful modelling of the interaction between matrix cracking and interface damage, especially during the initial stages of damage propagation, is achieved if the SCE adopted.

From the results presented, the merit of the proposed SCE over the traditional CE and approximate CE [27] formulations is that it provides a physically-based solution for correctly modelling interaction between matrix cracks and delamination. The kinematic compatibility is consistently enforced, leading to a more rigorous numerical formulation which is able to describe the local coupled failure mechanisms during the progressive damage process. Therefore, the SCE is a useful tool for high-fidelity modeling of failure patterns with delamination boundaries clearly bounded by matrix cracks.

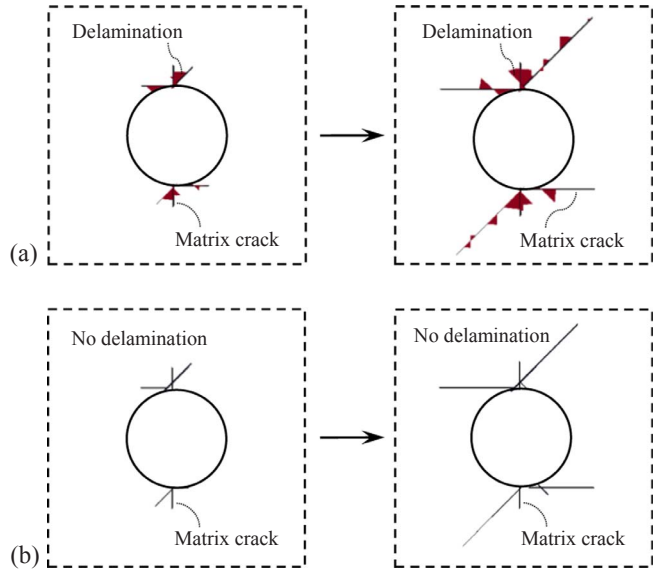

Fig. 19. Initiation of damage (left column) and subsequent propagation of damage shortly thereafter (right column): (a) SCE model with coupled matrix damage and delamination; (b) traditional CE model with only matrix cracking. (For interpretation of the references to colour in this figure legend, the reader is referred to the web version of this article.)

Acknowledgement

The first author greatly acknowledges the research scholarship and research grant (No. R265000523646) from the National University of Singapore.

References

[1] Johnson P, Chang FK. Characterization of matrix crack-induced laminate failure—Part I: experiments. J Compos Mater 2001;35(22):2009–35.
[2] Johnson P, Chang FK. Characterization of matrix crack-induced laminate failure—Part II: analysis and verifications. J Compos Mater 2001;35(22):2037–74.
[3] Hallett SR, Jiang WG, Khan B, Wisnom MR. Modelling the interaction between matrix cracks and delamination damage in scaled quasi-isotropic specimens. Compos Sci Technol 2008;68(1):80–9.
[4] Wisnom MR, Khan B, Hallett SR. Size effects in unnotched tensile strength of unidirectional and quasi-isotropic carbon/epoxy composites. Compos Struct 2008;84(1):21–8.
[5] Green BG, Wisnom MR, Hallett SR. An experimental investigation into the tensile strength scaling of notched composites. Compos Part A Appl Sci Manuf 2007;38(3):867–78.
[6] Hallett SR, Green BG, Jiang WG, Wisnom MR. An experimental and numerical investigation into the damage mechanisms in notched composites. Compos Part A Appl Sci Manuf 2009;40(5):613–24.
[7] Nixon-Pearson OJ, Hallett SR. An investigation into the damage development and residual strengths of open-hole specimens in fatigue. Compos Part A Appl Sci Manuf 2015;69:266–78.
[8] Zubillaga L, Turon A, Renart J, Costa J, Linde P. An experimental study on matrix crack induced delamination in composite laminates. Compos Struct 2015;127:10–7.
[9] Noh J, Whitcomb J. Prediction of delamination growth and opening near intersection of transverse matrix cracks and delamination. J Compos Mater 2005;39(15):1335–52.
[10] Dugdale DS. Yielding of steel sheets containing slits. J Mech Phys Solids 1960;8(2):100–4.
[11] Barenblatt GI. The mathematical theory of equilibrium cracks in brittle fracture. Adv Appl Mech 1962;7:55–129.
[12] Mi Y, Crisfield MA, Davies GAO, Hellweg HB. Progressive delamination using interface elements. J Compos Mater 1998;32(14):1246–72.
[13] Alfano G, Crisfield MA. Finite element interface models for the delamination analysis of laminated composites: mechanical and computational issues. Int J Numer Meth Engng 2001;50(7):1701–36.
[14] Turon A, Camanho PP, Costa J, Dávila CG. A damage model for the simulation of delamination in advanced composites under variable-mode loading. Mech Mater 2006;38(11):1072–89.
[15] Turon A, Davila CG, Camanho PP, Costa J. An engineering solution for mesh size effects in the simulation of delamination using cohesive zone models. Engng Fract Mech 2007;74(10):1665–82.
[16] Pinho S, Iannucci L, Robinson P. Physically based failure models and criteria for laminated fibre-reinforced composites with emphasis on fibre kinking. Part II: FE implementation. Compos Part A Appl Sci Manuf 2006;37(5):766–77.
[17] Song KC, Li YY, Rose CA. Continuum damage mechanics models for the analysis of progressive failure in open-hole tension laminates. In: 52nd AIAA/ASME/ASCE/AHS/ASC structures, structural dynamics and materials conference; 2011. p. 1861.
[18] Chen BY, Tay TE, Baiz PM, Pinho ST. Numerical analysis of size effects on open-hole tensile composite laminates. Compos Part A Appl Sci Manuf 2013;47:52–62.
[19] van der Meer FP, Sluys LJ. Continuum models for the analysis of progressive failure in composite laminates. J Compos Mater 2009;43(20):2131–56.
[20] Maimí P, Camanho PP, Mayugo JA, Dávila CG. A continuum damage model for composite laminates: Part I - Constitutive model. Mech Mater 2007;39(10):897–908.
[21] Iarve EV, Gurvich MR, Mollenhauer DH, Rose CA, Dávila CG. Mesh-independent matrix cracking and delamination modeling in laminated composites. Int J Numer Meth Engng 2011;88(8):749–73.
[22] Dolbow J, Belytschko T. A finite element method for crack growth without remeshing. Int J Numer Meth Engng 1999;46(1):131–50.
[23] Ling DS, Yang QD, Cox BN. An augmented finite element method for modeling arbitrary discontinuities in composite materials. Int J Fracture 2009;156(1):53–73.
[24] van der Meer FP, Sluys LJ. A phantom node formulation with mixed mode cohesive law for splitting in laminates. Int J Fracture 2009;158(2):107.
[25] van der Meer FP, Sluys LJ. Mesh-independent modeling of both distributed and discrete matrix cracking in interaction with delamination in composites. Engng Fract Mech 2010;77(4):719–35.
[26] Chen BY, Pinho ST, De Carvalho NV, Baiz PM, Tay TE. A floating node method for the modelling of discontinuities in composites. Engng Fract Mech 2014;127:104–34.
[27] Chen BY, Tay TE, Pinho ST, Tan VBC. Modelling the tensile failure of composites with the floating node method. Comput Methods Appl Mech Eng 2016;308:414–42.
[28] Chen BY, Tay TE, Pinho ST, Tan VBC. Modelling delamination migration in angle-ply laminates. Compos Sci Technol 2017;142:145–55.
[29] van der Meer FP. Mesolevel modeling of failure in composite laminates: constitutive, kinematic and algorithmic aspects. Arch Comput Methods Eng 2012;19(3):381–425.
[30] Tay TE, Sun XS, Tan VBC. Recent efforts toward modeling interactions of matrix cracks and delaminations: an integrated XFEM-CE approach. Adv Compos Mater 2014;23(5–6):391–408.
[31] Hu XF, Chen BY, Tirvaudey M, Tan VBC, Tay TE. Integrated XFEM-CE analysis of delamination migration in multi-directional composite laminates. Compos Part A Appl Sci Manuf 2016;90:161–73.
[32] Higuchi R, Okabe T, Nagashima T. Numerical simulation of progressive damage and failure in composite laminates using XFEM/CZM coupled approach. Compos Part A Appl Sci Manuf 2017;95:197–207.
[33] Fang XJ, Yang QD, Cox BN, Zhou ZQ. An augmented cohesive zone element for arbitrary crack coalescence and bifurcation in heterogeneous materials. Int J Numer Meth Engng 2011;88(9):841–61.
[34] De Carvalho NV, Chen BY, Pinho ST, Ratcliffe JG, Baiz PM, Tay TE. Modeling delamination migration in cross-ply tape laminates. Compos Part A Appl Sci Manuf 2015;71:192–203.
[35] Khoei AR, Moslemi H, Sharifi M. Three-dimensional cohesive fracture modeling of non-planar crack growth using adaptive FE technique. Int J Solids Struct 2012;49(17):2334–48.
[36] Park K, Paulino GH. Cohesive zone models: a critical review of traction-separation relationships across fracture surfaces. Appl Mech Rev 2011;64(6):060802.
[37] Yang QD, Schesser D, Niess M, Wright P, Mavrogordato MN, Sinclair I, et al. On crack initiation in notched, cross-plied polymer matrix composites. J Mech Phys Solids 2015;78(Suppl C):314–32.
[38] Harper PW, Hallett SR. Cohesive zone length in numerical simulations of composite delamination. Engng Fract Mech 2008;75(16):4774–92.
[39] Wisnom MR. Modelling discrete failures in composites with interface elements. Compos Part A Appl Sci Manuf 2010;41(7):795–805.
[40] van der Meer FP, Sluys LJ, Hallett SR, Wisnom MR. Computational modeling of complex failure mechanisms in laminates. J Compos Mater 2012;46(5):603–23.
[41] Chang KY, Llu S, Chang FK. Damage tolerance of laminated composites containing an open hole and subjected to tensile loadings. J Compos Mater 1991;25(3):274–301.